11th World Congress on Computational Mechanics (WCCM XI)
5th European Conference on Computational Mechanics (ECCM V)
6th European Conference on Computational Fluid Dynamics (ECFD VI)
July 20–25, 2014, Barcelona, Spain

DEMONSTRATION OF AUTOMATED CFD PROCESS USING MESHLESS TECHNOLOGY

Mohamed Yousuf[1], Munikrishna Nagaram[2], Parthiban Andavar[3] and Balakrishnan N.[4]

[1] Research Student, Indian Institute of Science, India, yousuf@aero.iisc.ernet.in
[2] Post-Doctoral Fellow, Indian Institute of Science, India, kishan@aero.iisc.ernet.in
[3] Project Engineer, S & I Engineering Solutions, India, parthiban@sandi.co.in
[4] Associate Professor, Aerospace Engineering, Indian Institute of Science, India, nbalak@aero.iisc.ernet.in

Key words: *meshless solver, Cartesian grid, CFD automation, store separation, flap deployment.*

In this paper, we have demonstrated an automated CFD process using Upwind- Least Squares Finite Difference (LSFD-U) meshless solver with the points generated by Cartesian grid methods. The point distributions around complex geometries are done easily and quickly without any human intervention. The entire sequence of the CFD process involving geometry redfinition, point generation and flow solution are carried out in an automated way in a scripted environment. Towards demonstrating a 2D automation process, a turbulent flow over a MDA-3 element is simulated for various flap positions using LSFD-U RANS solver. For the 3D demonstration, the store trajectory prediction is done using LSFD-U Euler solver. The complete trajectory prediction is automated by coupling the Cartesian grid generator, the LSFD-U solver and a 6-DOF simulator.

1 Introduction

Meshless solvers show a lot of promise in industrial computations involving complex geometries. One of the important reasons behind this expectation is, generating a set of points, needed for the meshless solvers, is expected to be easier as compared to discretizing the domain into non-overlapping volumes, as needed by the finite volume methodology. But till date, in the course of development of meshless methodologies, most of the significant works have assumed a point distribution from an established grid generator [1-4], with the exception of our earlier work [5], where the meshless solver LSFD-U is projected as a Cartesian grid method. Here the point distribution needed for the generalized finite

difference solver LSFD-U is obtained from a hybrid Cartesian grid. This way, limitations of the Cartesian grids as applied to a classical finite volume solver, like the appearance of small cut cells, are obviated, while the advantage in terms of automation is retained. Therefore, the work presented here can be considered as the logical next step in evolution of the LSFD-U solver, where its potential in an automated CFD process is demonstrated.

Two problems, one each in 2D and 3D, with representative geometric complexity, have been chosen for this demonstration. The 2D demonstration is towards optimizing the flap position of the MDA-3 element airfoil, for maximizing the cl_{max}. A CFD process for accomplishing this task, should be in a position to generate the grid (points distribution, in the present case) in an automated way, for every new position of the flap and the cl_{max} and α_{max} for this position are obtained by the repeated use of the flow solver for the entire range of α. Towards this objective, for a sequence of five flap positions, the solutions for a given flow condition are obtained in an automated way using the LSFD-U based RANS solver on a hybrid Cartesian point distribution.

For 3D demonstration, the inviscid LSFD-U solver is used for solving a store separation problem [11]. The flow solver is validated for store separation studies by simulating a sequence of five pre-defined store positions including the carriage position. The Cartesian point distributions are generated in an automated way and the store loads are computed using the LSFD-U solver. With this demonstration, the store trajectory is predicted by coupling the LSFD-U solver with a 6-DOF simulator and compared with the experimental results.

2 Numerical Procedure

Numerical procedure involves a complete coupling of point generator, flow solver and a 6-DOF simulator in case of the store separation study. The following sections briefly describe about point generation method, meshless solver and the equations solved for a rigid body motion.

2.1 Point Generation

The field points generation can be done easily and quickly around any complex geometries using a Cartesian grid method which divides the cells recursively until it resolves to the geometry. The input to the point generator can be a triangulated geometry for a full Cartesian grid (inviscid grid) or a viscous padding (boundary layer grids) wrapped around the body for a hybrid Cartesian grid. The recursive cell division continues until the nearbody field points spacing are comparable to the surface resolution of the body in their vicinity or the viscous padding front. The points are classified into groups based on the directionality exhibited by its neighbours in the local cloud [5]. A typical local cloud is shown in Figure 1.a. The points whose neighbours exhibit no directionality are classified as “general type”. The points are classified as “Cartesian type” where the

neighbours in the local cloud are aligned in x-y directions and "structured type" where the neighbours in the local cloud are aligned in ξ-η directions. For the general and Cartesian type points, the fluid flow governing equations are solved in x-y co-ordinate system and for the structured type points, equations are solved in the rotated co-ordinate systems. In general, the viscous padding which is wrapped around the body exhibits streamwise and normal directionality. The points inside the viscous padding fall under the category of structured type. The interface between the Cartesian front and viscous padding are treated as general type points and the Cartesian field points are Cartesian type. The Figure 1.b illustrates the region of all point types.

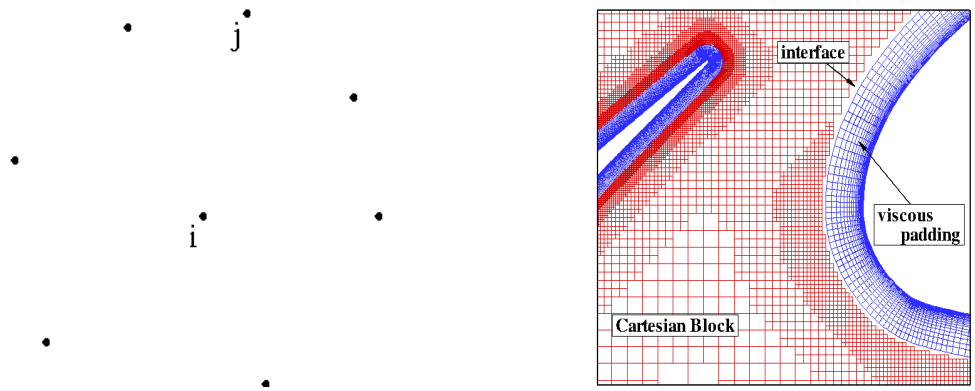

a. Typical local cloud b. View of hybrid Cartesian grid

Figure 1: Local cloud of "general type" point i and a typical hybrid Cartesian mesh

2.2 LSFD-U Flow Solver

The conservative form of 2D compressible Reynolds-Averaged Navier-Stokes equation can be expressed as follows:

$$\frac{\partial U}{\partial t} + \frac{\partial (F_I - F_V)}{\partial x} + \frac{\partial (G_I - G_V)}{\partial y} = 0 \tag{1}$$

where, conservative variable vector $U = \begin{bmatrix} \rho & \rho u & \rho v & e \end{bmatrix}^T$, F_I, G_I are the inviscid fluxes in the x and y direction, respectively, and F_V, G_V are the viscous fluxes in the x and y direction, respectively.

The flow solver employs the LSFD-U [2, 6] strategy, which is essentially an upwind generalized finite difference procedure based on the method of least squares. The solver incorporates an upwind procedure for discretizing the inviscid fluxes and robust viscous discretization strategy chosen based on the positivity for the viscous fluxes [7]. Higher order accuracy is achieved using a linear reconstruction procedure in conjunction with the Venkatakrishnan limiter [8]. The Spalart-Allmaras [9] turbulence model is employed for the transport of the eddy viscosity. The discretization strategy employed in the LSFD-U

solver exploits the directionality exhibited by the local cloud. The details of the discretization procedure can be had from references [5, 7]. Details of S-A model implementation are presented in reference [10].

2.3 6-DOF Model

The 6-DOF rigid body motion of the store, which includes 3 translations and 3 rotations, is calculated by numerically integrating Newton-Euler equations of motion. The translation and linear velocities of the store C.G is governed by Newton's laws of motion which are numerically integrated in the inertial frame of reference. The resultant forces acting on the store include aerodynamic forces, gravitational forces and external forces such as ejector forces. The resultant forces are kept constant over the discrete time interval of the integration. On the other hand, the angular motion of the store can be easily written in the body frame of reference. The resultant moments, which includes aerodynamic, ejector and damping, are transformed to the body frame of reference and kept constant over the discrete time interval. The Runge-Kutta 4th order time integration method is used for solving Euler equations of motion.

3 Results

3.1 MDA-3 Element Flap Deployment

One of the important steps in the design of a high lift system involves optimizing the flap/slat position for either maximum lift or mamimum lift to drag ratio. This inturn requires redefining the flap/slat positions repetitively within the bounds defined in a parametric space. The proposed CFD process is a demonstration towards automating this exercise using the meshless solver technology.

The turbulent flow past a MDA 30P-30N airfoil [12] is simulated at $M_\infty = 0.20$, $Re_\infty = 9.0 \text{ x } 10^6$ and an angle of incidence of 16.21^o. In the reference configuration (for which experimental results are available), flap is deployed by an angle of 30°. In order to demonstrate automation, the flap is deployed between 20° - 40° with the interval of 5°. This is illustrated in Figure 2.a and 2.b. Viscous padding grids are generated around each element and they are also allowed to move along with the geometry. Cartesian mesh is generated automatically for every new flap position. The automation cycle is briefly described in Figure 2.c. While the body has 5,300 points, the number of points in the hybrid grid is around 0.47 million. The hybrid Cartesian grid for the flap deployed at 30° is shown in Figure 2.d. Roe flux formula [13] is employed for the interface flux calculation.

Pressure and skin friction coefficients are plotted for all flap positions along with experimental values corresponding to the flap deployment of 30° in Figure 3.a and 3.b, respectively. The comparison shows good agreement with the experimental values available for

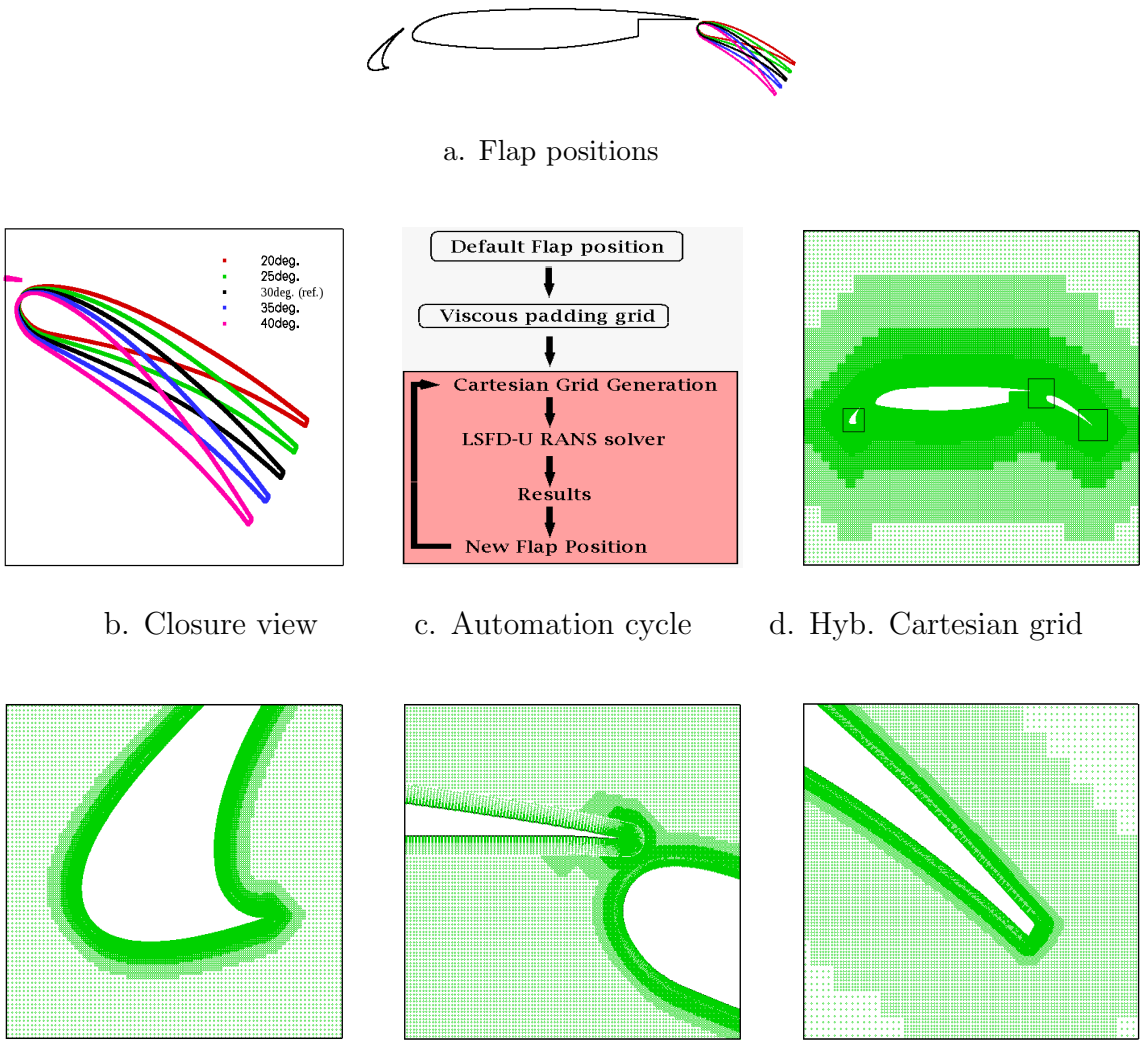

a. Flap positions

b. Closure view

c. Automation cycle

d. Hyb. Cartesian grid

e. Hybrid Cartesian grid (closure view)

Figure 2: Flap positions of MDA-3 element.

30° flap position. From the pressure distributions presented in Figure 3.a, it is clear that the flap is not stalled yet for the deflections considered and as a result experiences higher suction peaks and therefore greater lifts for progressively increasing flap deflections. The increase in the flap lift also results in an increased upwash at the slat and main element, further enhancing the lift experienced by these elements. This becomes further evident when we look at the lift variation against flap deflection presented in Figure 3.c. The lift and drag experienced by the high lift section for the standard 30 degree flap deflection case are compared with experimental data and the results obtained by HiFUN [14], an industrial standard finite volume solver in Figures 3.c and 3.d. A good prediction of the lift and over prediction of the drag by CFD for the case considered are in line with the available results from the literature [12, 15].

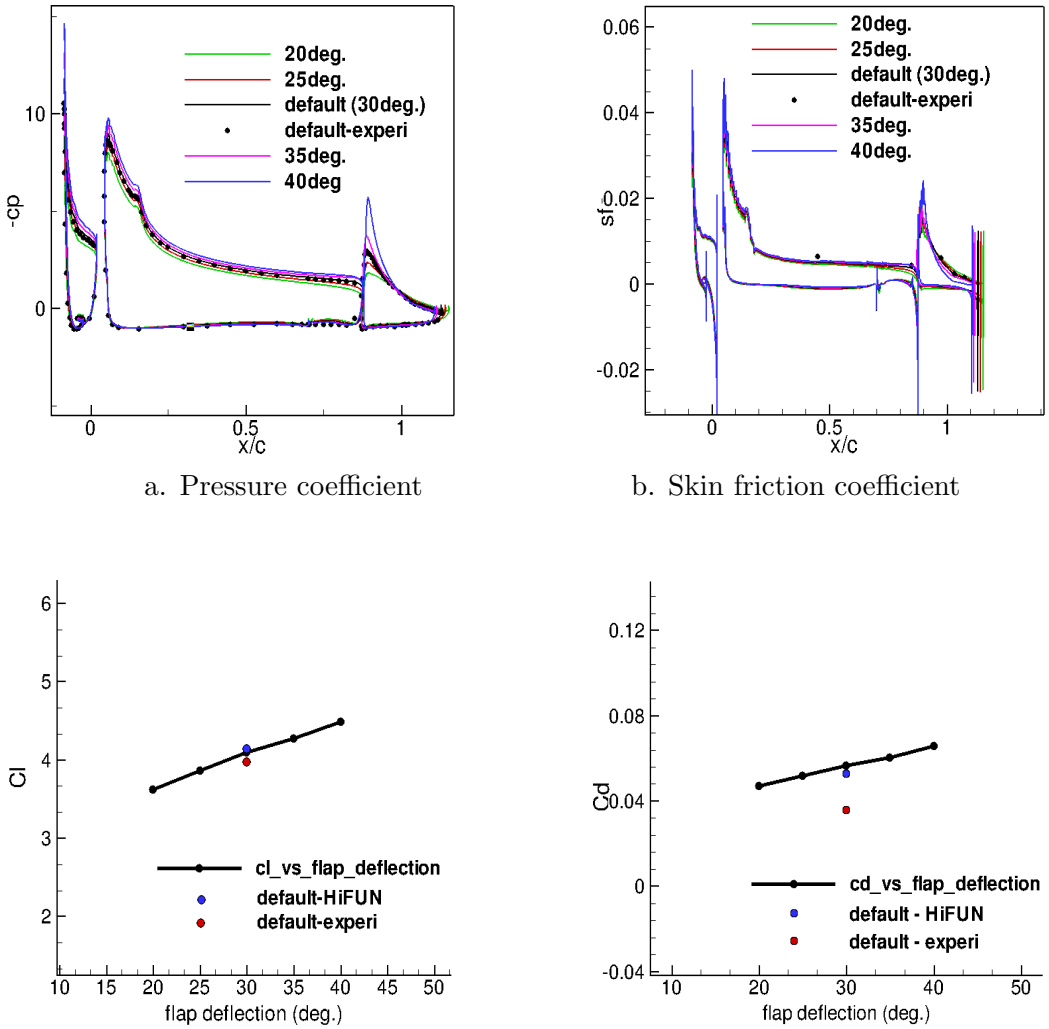

a. Pressure coefficient

b. Skin friction coefficient

c. Lift coefficient

d. Drag coefficient

Figure 3: MDA-3 Flap deployment study $M_\infty = 0.20$; AOA = 16.21^o; $Re_\infty = 9.0\text{x}10^6$

3.2 Store Trajectory Prediction

In order to demonstrate an automated process in 3D, a store separation study involving a generic wing, pylon and moving finned store [11] is considered. This experimental test case involves predicting the store loads and trajectory as obtained from a captive trajectory system for a duration of about 0.9s at 0.01s time intervals. For the purpose of validating flow solver for store separation studies, the methodology is demonstrated for a few pre-defined positions of the store and aerodynamic coefficients at these positions are compared with experimental data. The geometry of the wing and store considered for the problem is shown in Figure 4.a. Inviscid simulations are done for five pre-identified store positions for a freestream Mach number of 0.95 and a wing incidence of 0 degrees. The store positions are shown in Figure 4.b and a typical Cartesian grid around the wing and store geometry is shown in Figure 4.c. The experimental id, position number and

time after the store release for the selected pre-defined positions are tabulated in Table 1. While the surface grid is generated once with required fineness and is unchanged, the volume grid (point distribution) is regenerated for every store position. The surface grid has 126,233 points and 252,105 triangles. Apart from comparing the LSFD-U results with the available experimental data, an intercode comparison with a finite volume solver HiFUN is also presented. The volume grid details for all positions, as needed by the LSFD-U and the HiFUN solvers, are tabulated in Table 2. Inviscid fluxes are computed using vanLeer scheme [16] for these simulations.

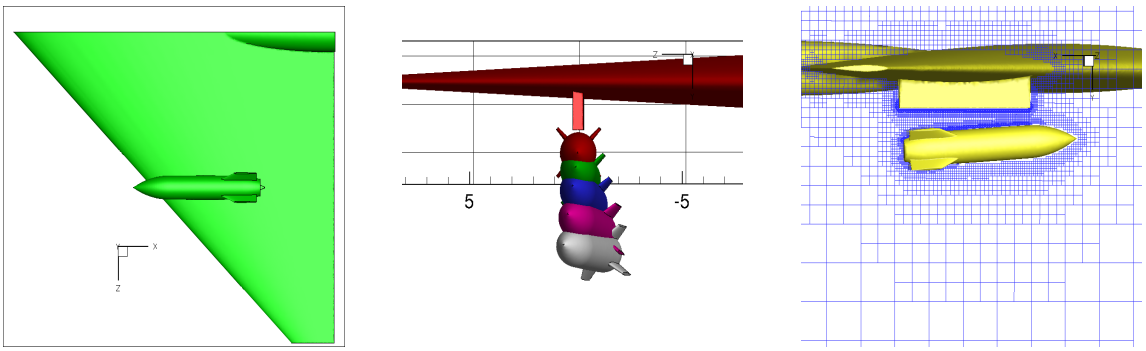

a. Geometry b. Store positions c. Cartesian grid

Figure 4: Store at pre-defined positions

Experimental ID	Positions	Time after store release (sec)
1	4	0.00
7	16	0.10
8	23	0.17
9	31	0.25
10	38	0.32

Table 1: Store positions and corresponding time

Experimental ID	Volume grid	
	Number of grid points (LSFD-U)	Number of cells (HiFUN)
1	1,645,030	3,298,474
7	1,713,043	3,092,507
8	1,718,914	3,160,202
9	1,730,551	3,200,055
10	1,729,110	3,222,079

Table 2: Grid information for all 5 store positions

The surface Mach and pressure fill plot for the store at carriage position are shown in Figure 5.a and 5.b, respectively. The pressure data on the wing surface is extracted at four

chord-wise sections, two inboard and two outboard locations as shown in Figure 6.a for comparing with experimental data. This sectional pressure data on the wing are compared with the experimental data and with the solution obtained using HiFUN in Figure 7. Though the sectional data obtained using CFD (both LSFD-U and HiFUN) show a good comparison with the experiments at pre-shock locations, the post-shock comparisons show larger deviations. This is possibly because of ignoring the shock-boundary layer effects in inviscid simulations. From an independent study involving RANS simulations using HiFUN we do have limited evidence to this effect. The axial pressure distribution on the store along the generators at different angular positions as depicted in Figure 6.b are compared with experimental and HiFUN data in Figure 8. The store pressure distribution obtained using the meshless solver shows an excellent comparison with the experimental data.

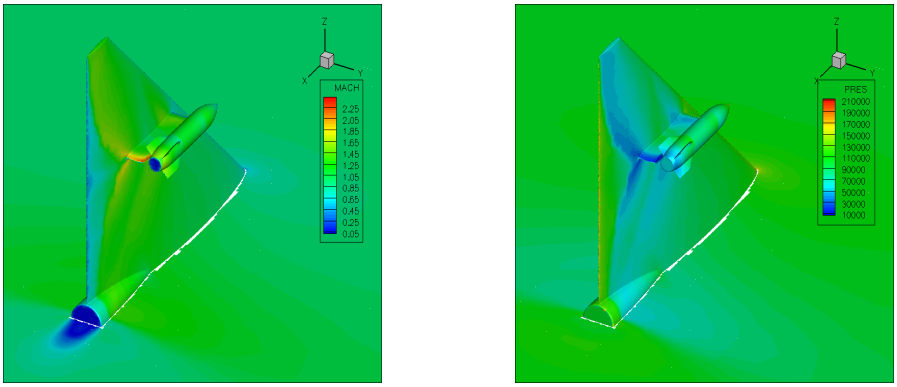

a. Mach Fill b. Pressure Fill

Figure 5: Store at carriage position: Mach = 0.95; AoA = 0 deg.

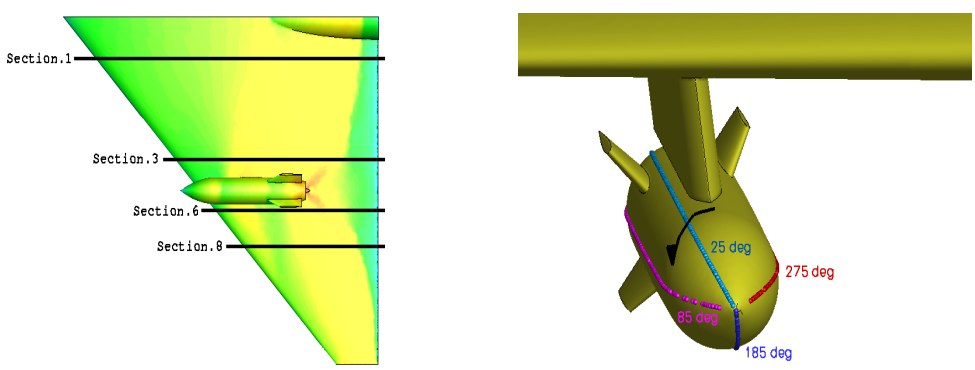

a. wing sectional locations b. store angular locations

Figure 6: Sectional locations for Cp extraction

With this surface pressure comparison of store at carriage position, the integrated force and moment coefficients are compared with experimental data and with HiFUN results for all five predefined positions. The sectional view of the Cartesian grid and the pressure

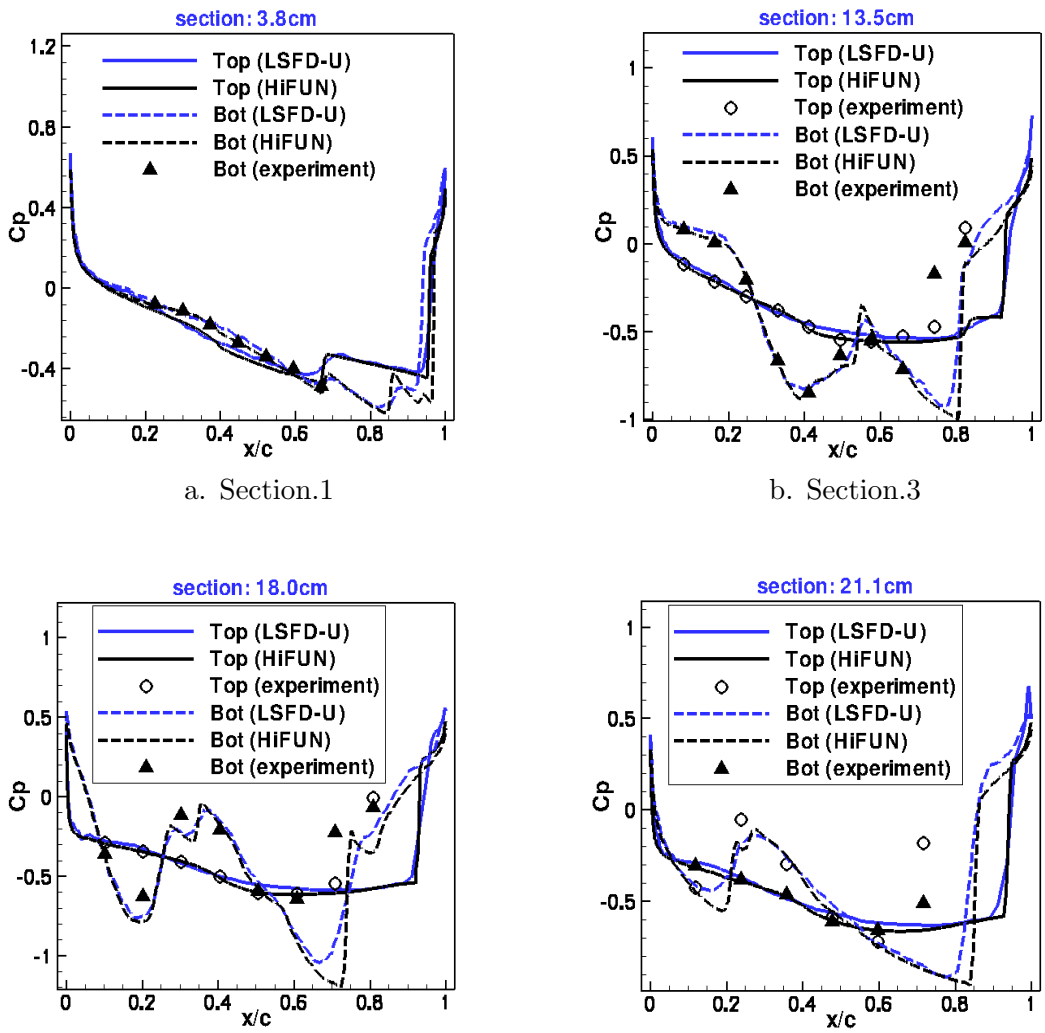

a. Section.1 b. Section.3

c. Section.6 d. Section.8

Figure 7: Wing sectional pressure coefficients for store at carriage position ($M_\infty = 0.95$, $\alpha = 0deg.$)

contours are shown in Figure 9 for all predefined experimental store positions. The axial, side and normal force coefficients from LSFD-U and HiFUN are plotted against the experimental predictions over a time range. The comparisons made in Figure 11.a show a good agreement with experimental data. Similar comparisons made for roll, pitch and yaw moment coefficients are shown in Figure 11.b.

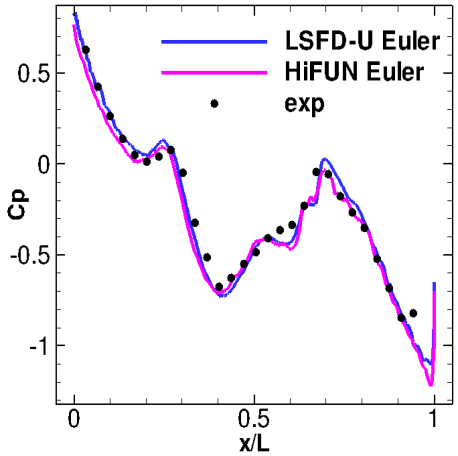

a. Angular Location - 25 degrees

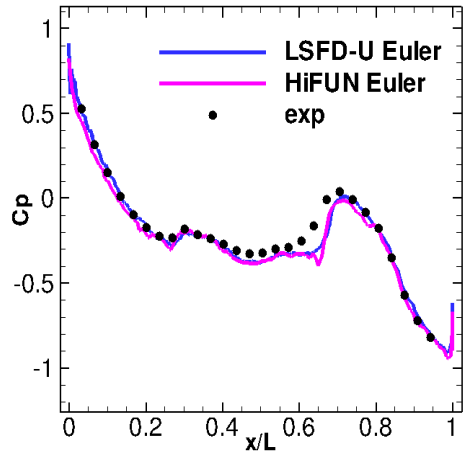

b. Angular Location - 85 degrees

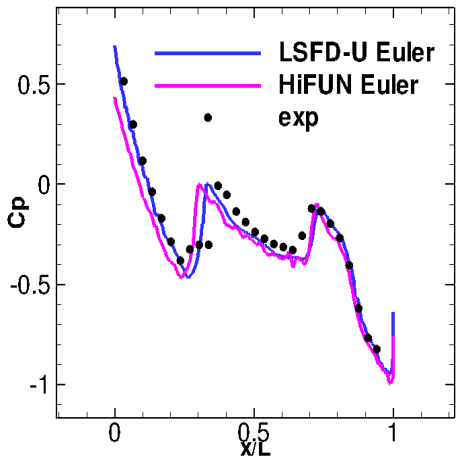

c. Angular Location - 185 degrees

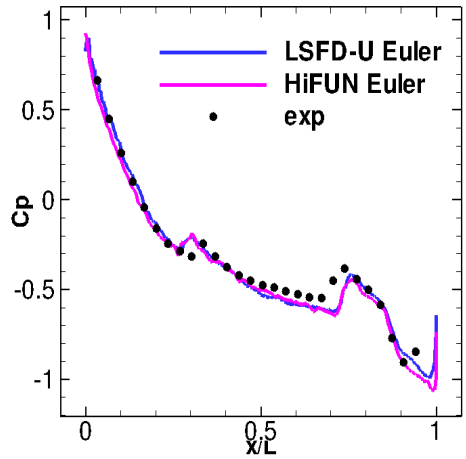

d. Angular Location - 275 degrees

Figure 8: Store angular pressure coefficients for store at carriage position ($M_\infty = 0.95$, $\alpha = 0deg.$)

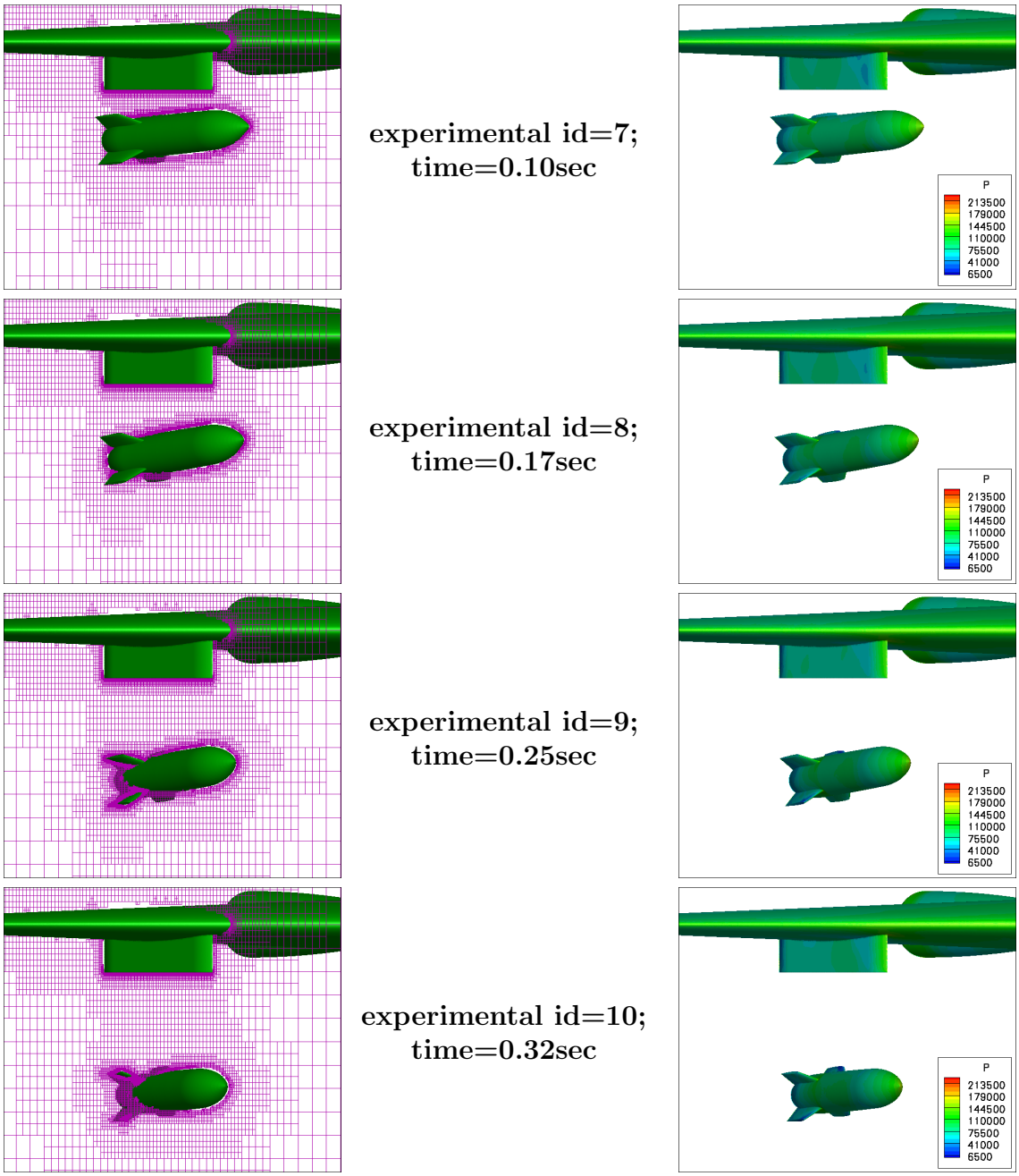

Figure 9: Sectional Cartesian grid and pressure contours for predefined store positions

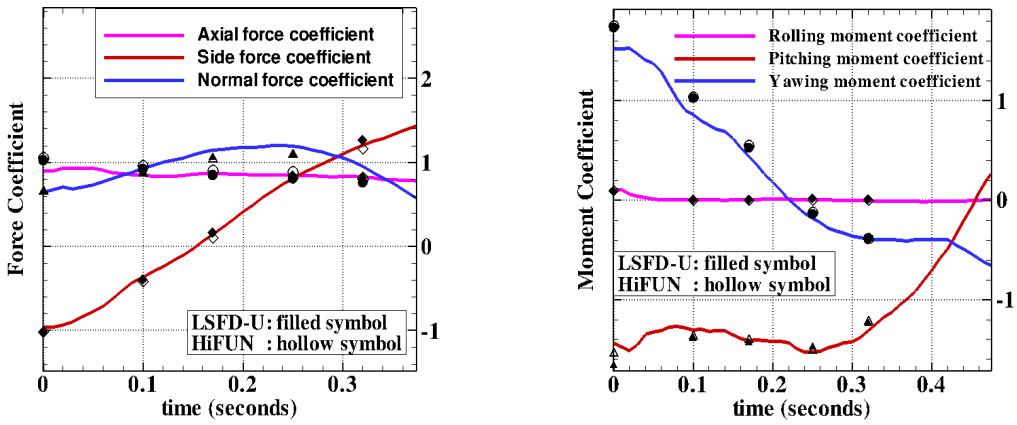

a. Integrated force coefficient b. Integrated moment coefficient

Figure 10: Integrated coefficients: plotted on experimental

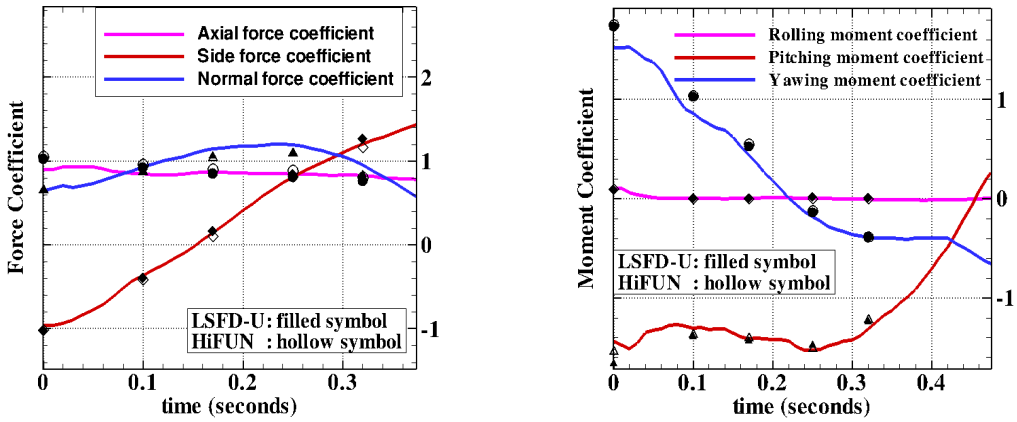

a. Integrated force coefficient b. Integrated moment coefficient

Figure 11: Integrated coefficients: plotted on experimental

After this successful validation, the LSFD-U Euler solver is coupled with a 6-DOF simulator for the complete store trajectory prediction. The process diagram of the automation cycle is shown in Figure 12. The store inertial characteristics are tabulated in Table 3. The constant ejector forces are applied on the store immediately after its release and are tabulated in Table 4. As described in automation cycle, the trajectory is computed using quasi-static approach using steady LSFD-U Euler solver. The simulations are carried out at a pressure altitude of 26000ft for a freestream Mach number of 0.95 and a wing incidence of 0 degrees. The surface pressure fill for few positions of the store are shown in Figure 13. The linear displacements and linear velocities of the store are the most critical parameters for ascertaining the safety of separation and deciding store envelope. The computed results of store linear displacements and relative linear velocities are compared with the experimental and HiFUN results and are shown in Figure 14.a and 14.b, respectively. The LSFD-U results are in excellent agreement with the experimental results. In Figure 14.c and 14.d, the store angular displacements and angular rates are compared with experimental and HiFUN results. The LSFD-U results are in good agreement with experimental results although there is a deviation in pitch angle and pitch rate beyond 0.3s. The axial, side and normal force coefficients are plotted with experiments and with HiFUN in Figure 15.a, and are in reasonable comparison with experimental predictions. Similarly, the roll, pitch and yaw moment coefficients compared in Figure 15.b. show reasonable comparison with experimental data, with yawing moment showing significant deviation from experiments beyond 0.3s. The LSFD-U results are similar to the results produced by HiFUN and other inviscid simulations [17, 18].

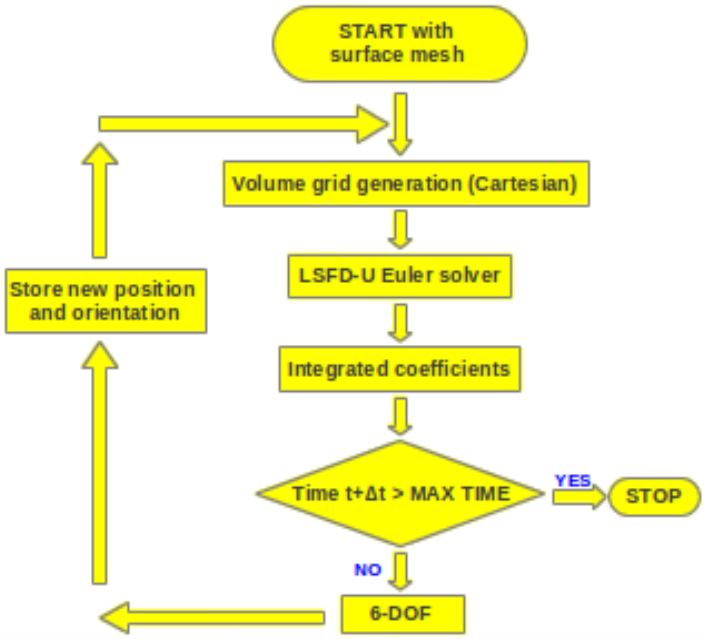

Figure 12: Process diagram of the automation cycle

Store mass	m=907.18 kg
Center of gravity	CG=1.416 m aft of store nose
Roll inertia	I_{XX}=27.12 $kg.m^2$
Pitch inertia	I_{YY}=488.1 $kg.m^2$
Yaw inertia	I_{ZZ}=488.1 $kg.m^2$
Other inertial properties	I_{XY}=I_{XZ}=I_{YZ}=0.0 $kg.m^2$
Roll damping coefficient	-4.0/rad
Pitch damping coefficient	-40.0/rad
Yaw damping coefficient	-40.0/rad

Table 3: Store characteristics

Forward ejector force	10675.7 N, constant
Forward ejector location	1.24 m aft of store nose
Aft ejector force	42702.9 N, constant
Aft ejector location	1.75 m aft of store nose
Ejector stroke length	0.10 m, approx. 0.054 sec after the store release

Table 4: Ejector characteristics

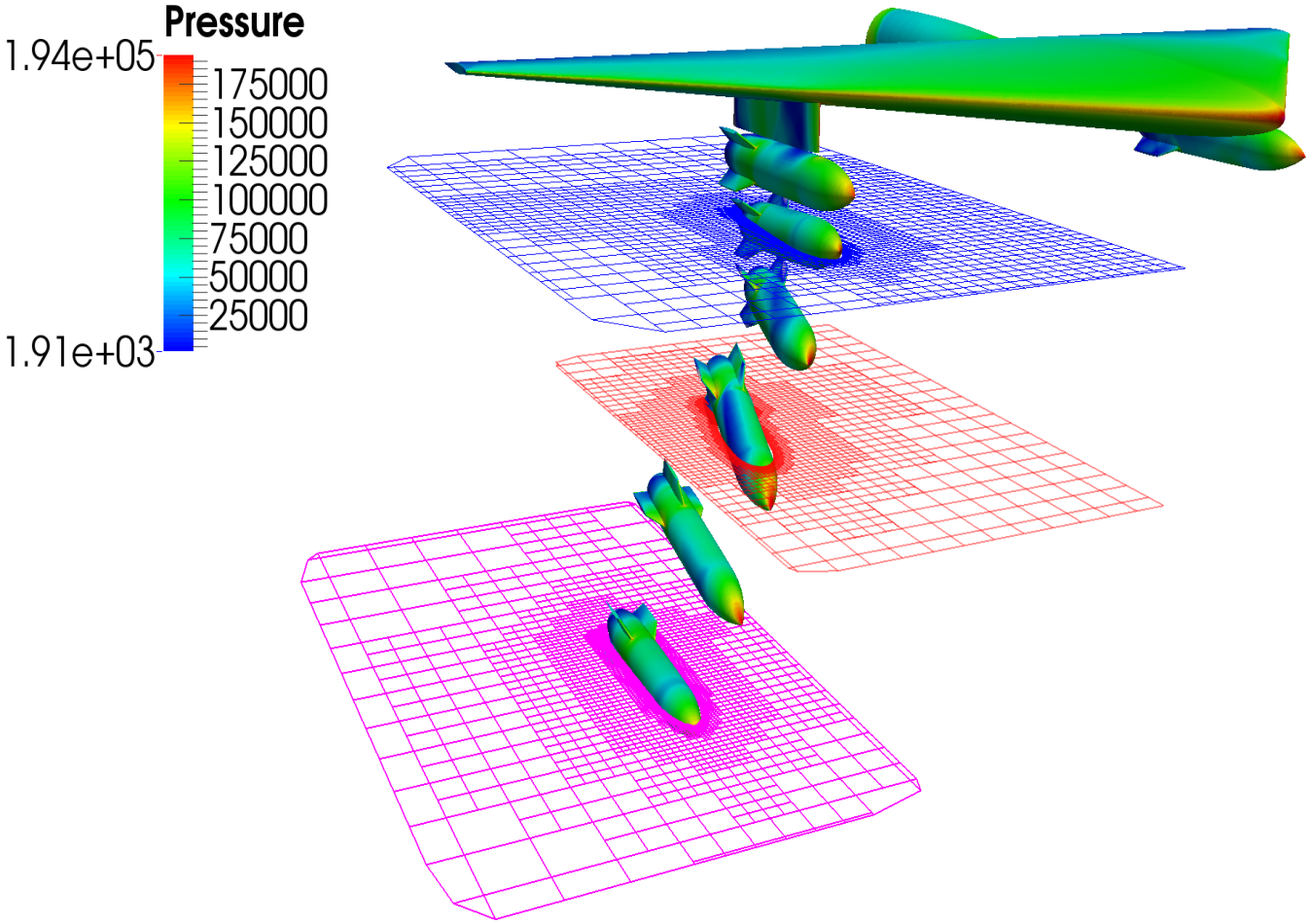

Figure 13: Pressure fill on the store surface at various time instants after its release (0.00sec, 0.20sec, 0.40sec, 0.60sec, 0.75sec and 0.89sec)

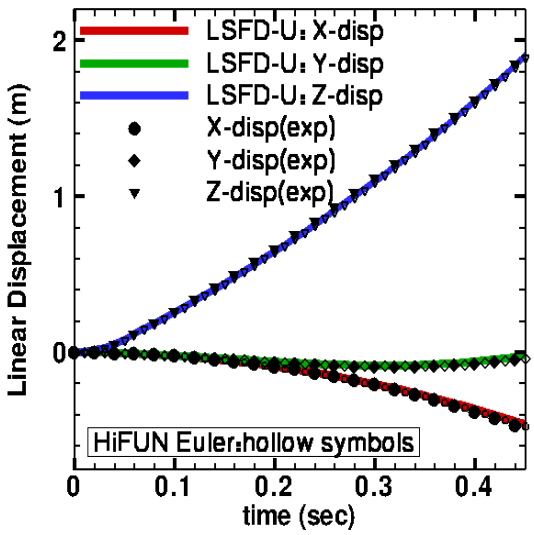

a. Linear displacements

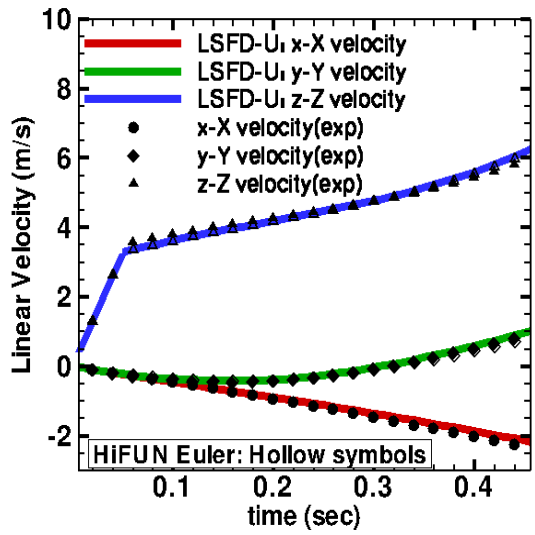

b. Relative linear velocities

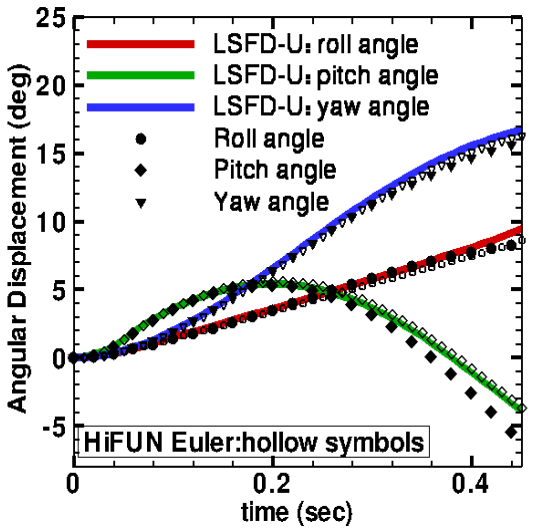

c. Angular displacements

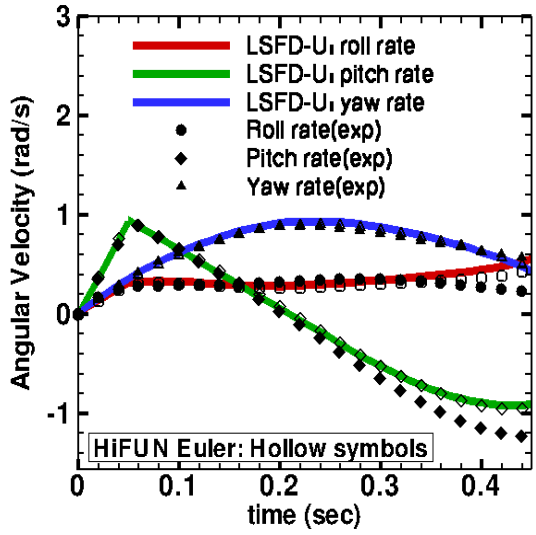

d. Angular rates

Figure 14: Linear and angular motions of the store after its release($M_\infty = 0.95$, $\alpha = 0deg.$)

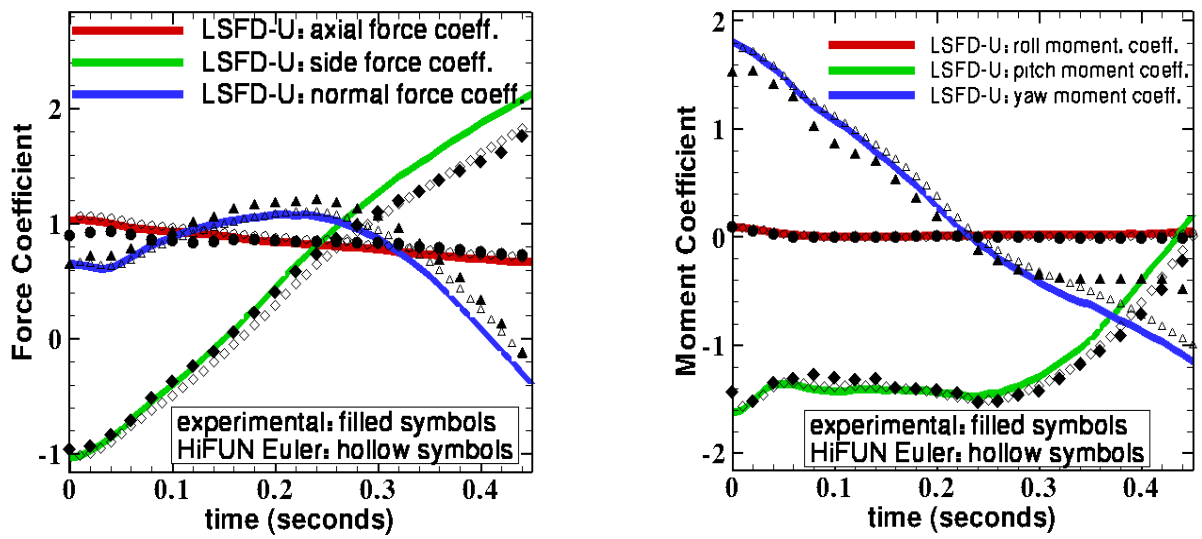

a. Force coefficients

b. Moment coefficients

Figure 15: Force and moment coefficients of the store after its release($M_\infty = 0.95$, $\alpha = 0deg.$)

Conclusions:

In this work, we have established an automated CFD process using the meshless LSFD-U solver along with an in-house Cartesian mesh generator. The numerical demonstrations presented clearly establish the utility of the meshless solver in the industrial applications requiring repeated geometry modification and grid (point) generation. The LSFD-U results for both flap deployment study and store trajectory prediction compare very well with the established finite voume based CFD tools, thus establishing the accuracy of the meshless solvers. The current efforts are towards understanding the differences presented by the CFD tools as compared to the experiments for the store separation study.

Acknowledgements:
The authors would like to thank Boeing for their support under the SID project PC36020. The authors also wish to thank Dr. Mori Mani, Boeing R & T, St. Louis, Dr. P. R. Viswanath, Boeing India, Bangalore, for their encouragement and constant support during the course of this work.

REFERENCES

[1] Ghosh A.K, Deshpande S.M., "Least squares kinetic upwind method for inviscid compressible flow", *AIAA Paper* 1995-1735; 1995.

[2] Sridar D and Balakrishnan N., "An upwind finite difference scheme for meshless solvers", *Journal of Computational Physics*, Vol. 189, pp. 1-23, 2003.

[3] Katz A. and Jameson A., "Meshless Scheme Based on Alignment Constraints", *AIAA Journal*, Vol.48, No.11, pp 2501-2511, 2010.

[4] Kennett, D.J., Timme, S., Angulo, J., and Badcock, K.J., "An Implicit Meshless Method for Application in Computational Fluid Dynamics". *International Journal for Numerical Methods in Fluids*, Vol. 71 issue 8 pp 1007-1028.

[5] Munikrishna N. and Balakrishnan N., "Turbulent flow computations on a hybrid Cartesian point distribution using meshless solver LSFD-U", *Computers and Fluids*, Vol. 23 , 2010.

[6] Balakrishnan N., "New least squares based finite difference method", *Report No.* 99 FM 9, Department of Aerospace Engineering, Indian Institute of Science, Bangalore, India, 1999.

[7] Munikrishna N., "On viscous flux discretization procedures for finite volume and meshless solvers", *Ph.D. Thesis*, Department of Aerospace Engineering, Indian Institute of Science, Bangalore, 2007.

[8] Venkatakrishnan V., "Convergence to steady state solutions of the Euler equations on unstructured grids with limiters", *Journal of Computational Physics*, Vol. 118, pp 120-130, 1995.

[9] Spalart, P. R. and Allmaras, S. R., "A One-Equation Turbulence Model for Aerodynamic Flows", *AIAA Paper* 92-0439, 1992.

[10] Munikrishna N., Mohamed Yousuf, Balakrishnan N., "Development of a 2D RANS LSFD-U Meshless Solver", *CAd Lab Technical Note*, CAd TN 2012:04, 2012.

[11] John H. Fox, Ph.D., "23. Generic Wing, Pylon and Moving Finned Store", *Sverdrup Technology, Inc./AEDC Group*, TR-026-23.

[12] Christopher L. Rumsey, Susan X. Ying, "Prediction of high lift: Review of present CFD capability", *Progress in Aerospace Sciences*, Vol, 38, pp. 145-180, 2002.

[13] Roe P.L., "Approximate Riemann solvers, parameter vectors and difference schemes", *Journal of Computational Physics*, Vol. 43:35772, 1981.

[14] "Simulation and Innovation Engineering Solutions Pvt. Ltd.", *http://www.sandi.co.in*.

[15] Christopher L. Rumsey et.al, "Three-Dimensional Effects on Multi-Element High Lift Computations", *AIAA 2002-0845*, 2002.

[16] van Leer B., "Flux Vector Splitting for Euler equations", ICASE Report No.82-30, Institute for Computer Applications in Science and Engineering, NASA Langley Research Center, Hampton, Virginia, 1982.

[17] Nichols .R .H, Tramel .R .W, "Applications of a Highly Efficient Numerical Method for Overset-Mesh Moving Body Problems", *AIAA 97-2255*, 1997.

[18] Torsten Berglind, Lars Tysell, "Numerical Investigation of the Impact of Maneuver on Store Separation Trajectories", *AIAA 2010-4241*, 2010.